Journal of Membrane Science 618 (2021) 118754

Contents lists available at ScienceDirect

Journal of Membrane Science

journal homepage: http://www.elsevier.com/locate/memsci

Stitching nanosheets of covalent organic frameworks to build aligned nanopores in nanofiltration membranes for precise ion separations

Zhe Zhang, Congcong Yin, Guanghui Yang, Ankang Xiao, Xiansong Shi, Weihong Xing, Yong Wang *

State Key Laboratory of Materials-Oriented Chemical Engineering, College of Chemical Engineering, Nanjing Tech University, Nanjing, 211816, PR China

ARTICLE INFO

Keywords:
Polyamide (PA)
Covalent organic frameworks (COFs)
Thin-film nanocomposite (TFN) membrane
Desalination

ABSTRACT

Embedding nanofillers into polyamide (PA) matrices is considered as a simple yet effective strategy for boosting the performances of thin-film nanocomposite (TFN) nanofiltration (NF) membranes. However, the NF performances are usually compromised by the inadequate interface compatibility between nanofillers and PA matrices as well as the anisotropic orientation of nanofillers. Herein, we propose a distinctive fabrication strategy for TFN membranes featuring excellent compatibility and highly-aligned microstructures. The reactive covalent organic framework (COF) nanosheets are chemically stitched at oil-water interfaces to form continuous nanofilms, and the PA matrices are then in-situ formed to encapsulate them, giving the TFN membranes. The stitched nanofilms contain two types of perpendicularly oriented pores: intrinsic apertures in COF nanosheets, and gaps among adjacent nanosheets. Together with the abundant reactive sites, the stitched nanofilms not only mediate the controllable synthesis of PA matrices, but also are covalently fused into the matrices. The aligned pores of the stitched nanosheets are capable of sieving salt ions, endowing TFN membranes with high separation precision and fast water permeation. This work demonstrates a strategy to control the orientation of COF nanosheets, which is highly desired in diverse fields not limited to membrane separation.

1. Introduction

The scarcity of clean water has become a globally pressing issue due to the continued water consumption and aggravated environmental contamination against the background of climate change, population booming and urban development [1]. Membrane separation technologies are of fundamental importance and great advantage for providing clean water compared to other separation technologies, benefiting from their high separation efficiency, low energy footprint and operational flexibility [2–4]. Nanofiltration (NF) is a flourishing membrane separation technique for water purification by means of which the small organics and multivalent salts can be excluded from water by the nanoscale membrane pores [5,6]. Polyamide (PA) thin film composite (TFC) membranes are a type of successfully commercialized and extensively utilized NF membranes thus far, which are fabricated by interfacial polymerization (IP). In a typical IP process, aqueous solutions containing amine monomers are pre-filled in porous substrates, and organic solutions containing acyl chlorides are subsequently added onto the substrate upper surfaces, triggering the IP processes [7,8]. The two polyfunctional monomers rapidly react at the interface of two immiscible phases to polymerize into PA nanofilms attaching onto the substrates, which is based on the Schotten-Baumann reaction [9,10]. However, such fast and irreversible IP would inevitably lead to ill-defined microstructures of PA layers including the intractable thickness and heterogeneous nanoporosity. Those TFC membranes would thus suffer from the sluggish water permeation or even the deficient solute selectivity [11,12]. Therefore, it still remains a great challenge for tackling such issues, particularly in an effective and affordable way.

Embedding nanofillers into PA matrices is recognized as a straightforward yet effective strategy to boost separation performances of PA layers without major changes to conventional IP processes. Nanofillers are usually pre-loaded on the upper surface of porous substrates, after which the PA layers are formed in-situ so that the nanofillers are encapsulated by the PA matrices to create thin-film nanocomposite (TFN) membranes [13]. The inherent pores, cavities, and stacked interspaces of the embedded nanofillers as well as the voids between PA matrices and nanofillers are employed as additional transport channels. Given this, these nanofillers could act as a performance enabler, which

* Corresponding author.
E-mail address: yongwang@njtech.edu.cn (Y. Wang).

https://doi.org/10.1016/j.memsci.2020.118754
Received 30 July 2020; Received in revised form 11 September 2020; Accepted 15 September 2020
Available online 22 September 2020

render TFN membranes fast water permeation, enhanced separation precision or both. Since the first attempt made in 2007 [14], numerous nanomaterials have been used as fillers to dope into PA layers, and they can be categorized as non-porous and porous nanofillers. Non-porous nanomaterials including silica [15], quantum dots [16], graphene oxide (GO) [17], attapulgite [18], and MoS_2 [19], are reported examples used for TFN membranes. The incorporation of non-porous nanomaterials would lead to the partial reduction of the intertwining intensities of the highly cross-linked polymer chains inside PA matrices to some extent, creating abundant tiny nanovoids between those nanomaterials and PA matrices. Thereby, these nanovoids function as the additional transport channels for water permeation and solutes sieving. Besides, the stacks of two-dimensional (2D) nanomaterials such as GO and analogues thereof can be integrally embedded into PA, forming relatively disordered or somewhat aligned architectures inside. The nanosized interspaces of the stacked 2D materials thus could also serve as the transport channels. In another scenario, porous nanomaterials such as zeolites [14], metal-organic frameworks (MOFs) [20], and covalent organic frameworks (COFs) [21,22], and polymersomes [23,24] are promising categories of fillers featuring high porosities or large cavities. In addition to the nanovoids which is similar to that of non-porous nanofillers, their inherent pores and cavities can be directly used as the transport channels, enabling much faster water permeation.

However, two major obstacles in fabricating high-performance TFN membranes are yet remaining. The first is the interfacial compatibility between the nanofillers and PA matrices. The compatibility between inorganic fillers/inorganic-organic hybrids and pure organic PA matrices are major concerns during the fabrication processes. The natively vulnerable compatibility of those materials would lead to non-selective voids, thus deeply compromising the separation precision. Although some pure organic nanofillers seem to be effective for enhancing the compatibility, the separation precision is usually unsatisfied. For instance, the divalent salts rejections of TFN membranes embedded with pure organic nanofillers are usually lower than 95% [21,24–26]. The second is the alignment of the nanofillers inside the PA matrices, which is of vital significance to separation precision. Highly-aligned nanofillers may produce more regular and preferentially oriented nanochannels for faster water permeation and enhanced solutes sieving properties compared to that of randomly-aligned nanofillers [13]. Besides, alignment could overcome the agglomeration of nanofillers, preventing the negative effects on separation performance. Aligning nanofillers onto the porous substrates prior to the IP, is the mostly adopted protocol to produce the preferentially aligned structures within PA matrices. However, this method is yet limited, as the pre-aligned nanofillers may become much disordered when facing the addition of organic solutions during the IP processes. To this end, should interfacial compatibility and preferential alignment of the nanofillers be fully implemented, the TFN membranes would be expected to meet the demand of high-efficient NF applications.

2D COFs, a regime of porous and crystalline framework materials, are constructed from the reticular chemistries, in which the pure organic structural motifs are covalently bonded and extended to periodically ordered architectures [27,28]. 2D COFs are eminent over their ordered apertures, entirely organic backbones, large surface areas, extremely low density, and vast possibilities for functionalization [28]. In the case of the TFN membranes fabrication, those distinctive superiorities may offer excellent interfacial compatibility and more regular alignment inside PA matrices. 2D COFs are thus expected as a promising type of nanofillers for fabricating high-performance TFN membranes. Herein, we proposed a unique fabrication strategy for TFN membranes featuring both fast water permeation and high separation precision (Scheme 1 and Fig. S1). Amino-COF nanosheets were chemically stitched to form a highly-aligned architecture at an oil-water interface by a reaction-diffusion driven synthesis (RDDS), the apertures of which were facing to the perpendicular direction. During the stitch process, individual COF nanosheets were covalently interlinked and integrated to form continuous thin films via the reactions between the trimesoyl chloride and the amino groups of COF nanosheets. The TFN membranes were then constructed by introducing the piperazine (PIP) into the aqueous solutions, producing a composite comprising aligned COF and PA. The intrinsic apertures in COF nanosheets and the stitched gaps among adjacent nanosheets can mediate the IP process via retarding the diffusion of PIP molecules toward organic solutions, leading to ultrathin thicknesses and patterned surfaces. Besides, those pores also acted as a rectifier, by means of which the inorganic salts of Na_2SO_4 and NaCl can be selectively sieved. This work provides an unusual strategy for the design and fabrication of TFN membranes by aligning the compatible, porous, and customizable COF nanosheets into PA matrices for

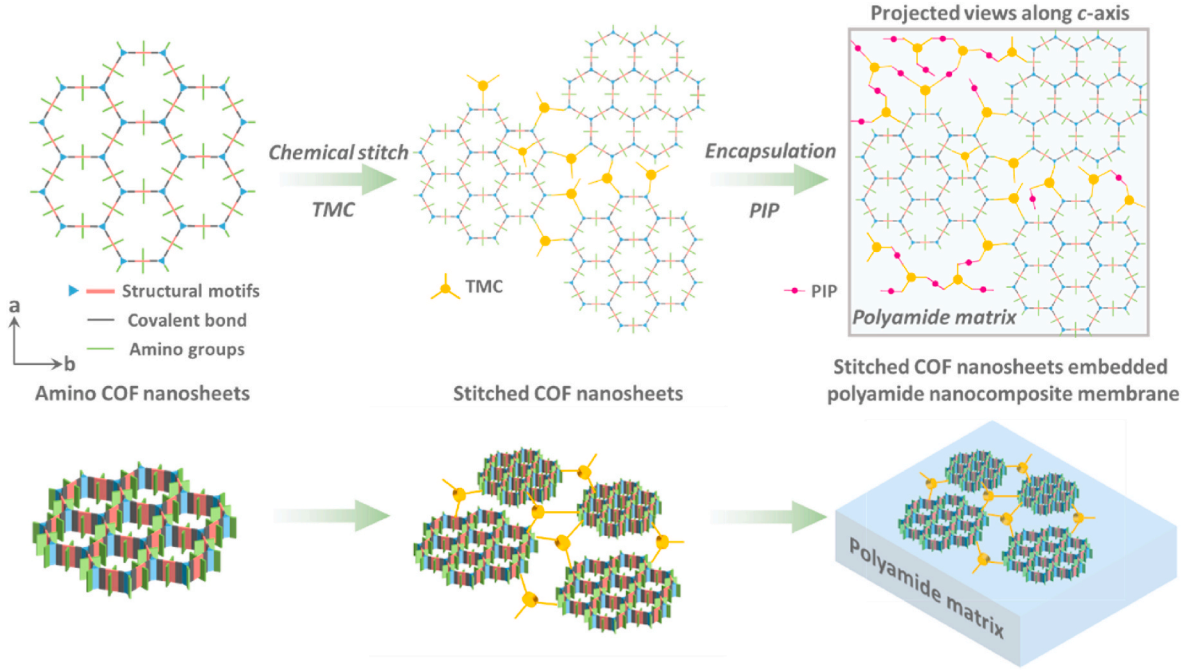

Scheme 1. Schematic illustration of the fabrication of TFN membranes.

high-efficient NF applications.

2. Experimental section

2.1. Materials

Unless otherwise mentioned, all chemicals used in this work were analytical grade. 1,3,5-Triformylphloroglucinol (Tp, 95%, TongChuangYuan Pharmaceutical), 3,3′-dinitrobenzidine (BD-NO_2, 95%, TCI), tin (II) chloride dihydrate ($SnCl_2{\cdot}2H_2O$, 99%, Macklin), trimesoyl chloride (TMC, 98%, Sigma-Aldrich), 4-(dimethylamino) pyridine (DMAP, 99%, Sigma-Aldrich), and anhydrous piperazine (PIP, 99%, Alfa Aesar) were used without further purification. Other reagents including solvents and inorganic salts were commercially available and used as received. Polyacrylonitrile (PAN, Mw = 150,000 Da) was used to fabricate porous substrates. Deionized water (Wahaha Group Co., Ltd.) was used throughout the whole work.

2.2. Synthesis of TpBD-NO_2

TpBD-NO_2 was synthesized under the solvothermal conditions which was reported by Banerjee and co-workers with some modifications [29]. In the typical synthesis, to a 25 mL Schlenk tube, 0.3 mmol of Tp, 0.45 mmmol of BD-NO_2, 5 mL of mesitylene, 5 mL of 1,4-dioxane, and 1 mL of 9 M aqueous acetic acid were added successively. The mixture was then sonicated for 5 min to ensure good dispersion. The tube was flash frozen in liquid nitrogen, degassed by three freeze-pump-thaw cycles, and sealed off. The reaction mixture was heated at 120 °C for 72 h. The red precipitates were collected by filtration and washed with tetrahydrofuran (THF). In order to fully remove the residual solvent molecules and oligomers, raw products were further subjected to Soxhlet extraction using THF as the solvent for at least 24 h. The resultant powders were isolated by filtration and vacuum dried at 120 °C for 12 h to afford the final products.

2.3. Synthesis of TpBD-NH_2

TpBD-NH_2 was synthesized by the chemical reduction of TpBD-NO_2, which was previously reported by Bein and co-workers [30]. Typically, 3 g of $SnCl_2{\cdot}2H_2O$, 5 mL of anhydrous THF, and 150 mg of TpBD-NO_2 powder were added into a 100 mL round-bottom flask in sequence. The reaction mixture was then vigorously stirred, refluxed at 80 °C for 5 h. The dark red precipitates were filtrated and thoroughly washed with 1 M hydrochloric acid, water, and ethanol. The resultant powders were vacuum dried at 120 °C for 12 h to afford the final products.

2.4. Liquid exfoliation of TpBD-NH_2

TpBD-NH_2 nanosheets were prepared by sonication-assisted liquid exfoliation. Briefly, 500 mg of TpBD-NH_2 powders were dispersed into a 500 mL glass bottle charging with 500 mL of water. The mixture was subjected to a tip-sonication with an output power of 600 W for 3 h. Afterward, the mixture was centrifuged (8000 rpm, 5 min) and the supernatants were collected as the final nanosheets dispersion (concentration was ~0.01 mg mL^{-1}).

2.5. Membranes fabrication

Prior to the fabrication of various membranes, the PAN porous substrates were prepared by the non-solvent induced phase separation method. Briefly, a certain amount of PAN powders and *N*, *N*-dimethylformamide were added into a 100 mL flask (the concentration of PAN was 12 wt%). The mixture was mechanically stirred at 70 °C for 5 h to form a homogeneous dope solution, and stood over night to fully release the trapped tiny air bubbles. The dope solution was poured-out onto the nonwoven fabrics followed by spreading it using a casting-knife with a fixed height of 200 μm on an automatic film applicator. Once the dope solution is spread, the polymer-coated nonwoven fabrics were quickly immersed into water bath for the coagulation. The water permeance of the resultant PAN substrate membranes was ~1000 L m^{-2} h^{-1} bar^{-1} and substrates were stored in water for further use.

The fabrication of TFN membranes involves two steps as shown in Fig. S1. The first step was the formation of TpBD-NH_2 nanofilms at oil-water interfaces. The second step was the in-situ formation of PA matrices in which certain amounts of PIP solutions was introduced into the aqueous solutions to form the final TFN membranes comprising PA matrices and TpBD-NH_2. In the first step, TpBD-NH_2 nanofilms were prepared by a reaction-diffusion driven synthesis (RDDS) at oil-water interfaces. In a typical process, a clean glass plate (6 cm × 6 cm) was horizontally placed in a Petri dish with a diameter of 9 cm. 20 mL of the aqueous solutions (water as the solvent) containing 0.2 mg mL^{-1} of DMAP (catalyst) and 0.01 mg mL^{-1} TpBD-NH_2 nanosheets were added. Afterward, 20 mL of the organic solutions (*n*-hexane as the solvent) containing 3 mg mL^{-1} of TMC were slowly added onto the aqueous solutions to initiate the reaction. It is notable that the high TMC concentration would make the reactions proceed thoroughly. The reaction lasted for 15, 30, 60, 180 and 600 s, respectively. The nanofilms formed at the interfaces were fished up using the pre-set glass plate, and then transferred into a water bath to release the nanofilm, further relieving the residual stresses within the nanofilms. Finally, the nanofilms floating on water were transferred onto silicon wafers or composited with PVDF macroporous substrates and heated under 60 °C for 10 min to enhance the adhesion. Nanofilms formed at 30 s were used for further characterizations.

In the second step, the construction of TFN membranes begins after a period of 30 s when the organic solutions completely contacted with the aqueous solutions. At 30 s as mentioned above, 5 mL of PIP aqueous solutions with various concentrations were carefully injected along the edge of the Petri dish into the former aqueous solutions by using a syringe (the injection was finished within 30 s). After the injection, concentrations of PIP in aqueous solutions were 0.125, 0.25, 0.5, 1 and 2 mg mL^{-1}, respectively. The reaction lasted for another 5 min to make sure the PA matrices were completely formed. Other steps were the same as the construction procedures of TpBD-NH_2 nanofilms. The constructed TFN membranes were named as COF-PA. To conduct a comparison, two control membranes named PA and FreeCOF-PA were also fabricated. PA membranes were formed by the IP between an aqueous solution containing PIP (0.5 mg mL^{-1}) and DMAP (0.2 mg mL^{-1}), with an organic solution containing TMC (3 mg mL^{-1}). FreeCOF-PA membranes were formed by the IP between an aqueous solution containing TpBD-NH_2 nanosheets (0.01 mg mL^{-1}), PIP (0.5 mg mL^{-1}), and DMAP (0.2 mg mL^{-1}), with an organic solution containing TMC (3 mg mL^{-1}). These two reactions both lasted for 5 min and other procedures were the same as previous.

2.6. Characterizations

Fourier transform infrared spectrometer (FT-IR, Nicolet 8700, Thermo Fisher Scientific) was used to reveal the chemical compositions of COFs and membranes. Powders samples were prepared by potassium bromide tablets, while the membranes samples were tested using an attenuated total reflectance (ATR) accessory. X-ray diffraction (XRD) patterns of COFs were collected on a diffractometer (Smart Lab, Rigaku). The scanning range (2θ) was started from 2 to 30°, and the scanning step was 0.02° s^{-1}. Field-emission scanning electron microscopy (FE-SEM) images of samples were obtained on a S-4800 microscope (Hitachi) with an accelerating voltage of 3 kV. Before imaging, all samples were ion-sputtered with an ultrathin layer of gold to enhance their conductivity. High-resolution transmission electron microscope (HRTEM) images were recorded from a Tecnai G2 F30 *S*-Twin microscope (FEI), which was operated at 300 kV. Sample was prepared by solvent evaporation of the nanosheets dispersion after it drop-coated on a carbon film covered

copper grid. Atomic force microscopy (AFM, XE-100, Park Systems) was used to collect the height profiles of the membranes. Samples were prepared by fishing up the membranes from water and transferring them onto silicon wafers. Water contact angles (WCAs) of membranes were obtained by a goniometer (Drop Meter A100P, MAIST). The streaming potentials testing of membranes were conducted on an electrokinetic analyzer (SurPASS, Anton Paar GmbH). A background electrolyte solution of KCl (0.1 mM) was used, and the pH values were controlled by adding 0.1 M sodium hydroxide and hydrochloric acid throughout the test, respectively.

2.7. Desalination performance evaluation

The desalination performances of various membranes were evaluated on a lab-scale cross-flow NF system with three stainless-steel testing cells connected parallelly. The active membrane area was 7.1 cm^2. The hydraulic pressure across the membrane during the test was maintained at 4 bar, and the liquid flow rate was fixed at 30 L h^{-1}. The solution temperature was regulated by a heat exchanger at 25 °C. Prior to the testing, all membranes were stabilized at a pressure of 5 bar for at least 45 min. The concentration of all inorganic salt solutions adopted in the test was 1000 ppm.

The permeation flux (J, L m^{-2} h^{-1}) and permeance (L m^{-2} h^{-1} bar^{-1}) were calculated as follows:

$$J = \Delta V / (A\ \Delta t) \quad (1)$$

$$Permeance = J / \Delta p \quad (2)$$

where ΔV (L) is the volume of the permeated solution, A (m^2) is the active membrane area, Δt (h) is the permeating time, and Δp (bar) is the transmembrane pressure used during the test.

The inorganic salt rejection rate (R, %) and the separation factor of NaCl to Na_2SO_4 (α) were calculated as follows:

$$R = (1 - C_p / C_f) \times 100\% \quad (3)$$

$$\alpha = (1 - R_{NaCl})/(1 - R_{Na_2SO_4}) \quad (4)$$

where C_p and C_f are the concentrations of the permeated and feed solutions, respectively. The concentrations of solutions were calculated from an electrical conductivity meter (S230–K, Mettler-Toledo).

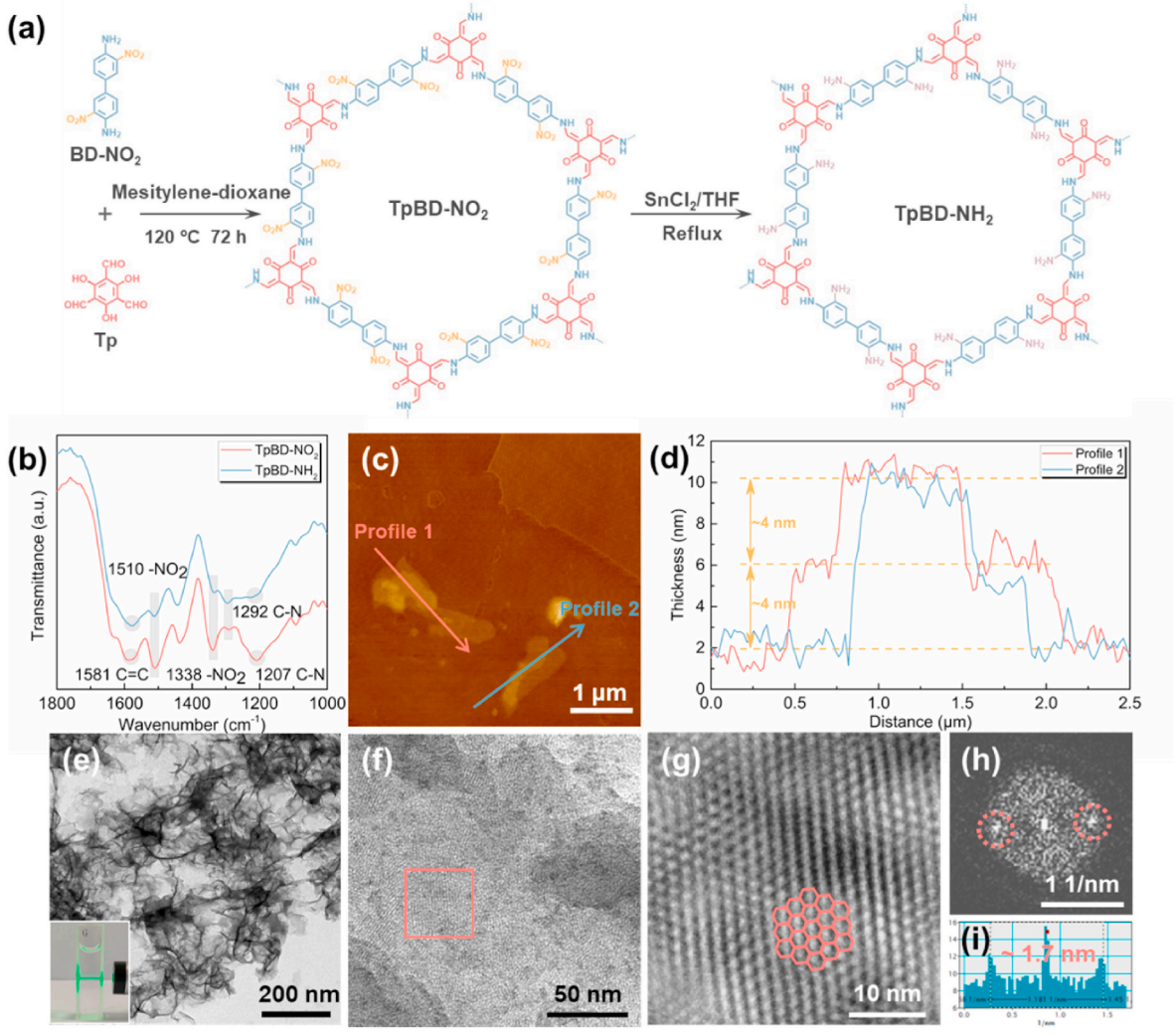

Fig. 1. Characterizations of TpBD-NO_2 and TpBD-NH_2 nanosheets. (a) Synthesis and reduction processes of TpBD-NO_2 and TpBD-NH_2. (b) FT-IR spectra of TpBD-NO_2 and TpBD-NH_2. (c) AFM image of TpBD-NH_2 nanosheets. (d) Height profiles of TpBD-NH_2 nanosheets corresponding to the two lines marked in (c). (e) HRTEM image of TpBD-NH_2 nanosheets in low magnification (Inset shows the Tyndall effect of TpBD-NH_2 nanosheets dispersion). (f) HRTEM image of TpBD-NH_2 nanosheets in high magnification. (g) FFT-filtered HRTEM image of TpBD-NH_2 nanosheets corresponding to the area marked in (f) (inset shows a lattice model of TpBD-NH_2). (h) FFT image of TpBD-NH_2 nanosheets corresponding to the area marked in (f). (i) Distance profile of the two adjacent diffraction spots which are marked in (h).

3. Results and discussion

3.1. Characterization of TpBD-NH_2 nanosheets

In this work, a β-ketoenamine-linked COF TpBD-NH_2 were chosen as the nanofiller for the fabrication of TFN membranes. The β-ketoenamine linkage is distinguished for its high chemical and thermal stabilities especially in acidic and alkaline environments [29,31]. Because the crystalline TpBD-NH_2 are not able to be directly synthesized from Tp and 3,3′-diaminobenzidine (BD-NH_2), a stepwise method was adopted [30]. As shown in Fig. 1a, TpBD-NO_2 was firstly synthesized from Tp and BD-NO_2 under a solvothermal condition, and then chemically reduced to TpBD-NH_2 by $SnCl_2$. The chemical compositions of TpBD-NO_2 and TpBD-NH_2 were confirmed by the FT-IR spectra (Fig. 1b). The presence of the stretching vibration peaks of C═C (1581 cm^{-1}) and C–N (1292 cm^{-1} and 1207 cm^{-1}) indicates the formation of the β-ketoenamine linkage. Moreover, after the reduction, the symmetric and asymmetric stretching vibration peaks of –NO_2 located at 1338 and 1510 cm^{-1} in TpBD-NH_2 spectrum were significantly weakened, and the stretching vibration peak of C–N (1292 cm^{-1}) was enhanced. These results evidence that the TpBD-NO_2 and TpBD-NH_2 were successfully synthesized and the nitro groups are effectively converted into amino groups.

The morphologies of TpBD-NO_2 and TpBD-NH_2 bulks were observed by SEM (Fig. S2). Both COFs exhibit a spherical structure composed of massive nanoribbons, and the diameters of spheres are several microns. The nanosheets of TpBD-NH_2 can be obtained after a sonication-assisted liquid exfoliation, and their thicknesses were measured form the AFM image (Fig. 1c and d). The height profiles in Fig. 1 d demonstrate that the average thickness of the nanosheet was ~4 nm. Besides, their maximum lateral sizes are a few microns (Fig. 1c). To obtain further information on the crystalline characteristics of TpBD-NH_2 nanosheets, the HRTEM imaging was conducted. As shown in Fig. 1e–i the TpBD-NH_2 nanosheets exhibit a wrinkle morphology with a low magnification (Fig. 1e). Under high magnification, we observed a large area of lattice fringes, which belong to the (100) crystallographic plane (Fig. 1f). Furthermore, that information was smoothed and filtered by the fast Fourier transform (FFT), and a highly ordered microdomain (40 nm × 40 nm) with the aligned lattice fringes were obtained (Fig. 1g). These results indicate that the TpBD-NH_2 nanosheets are highly crystalline which is consistent with that from the XRD patterns (Fig. S3). Besides, based on the distance between two adjacent diffraction spots shown in Fig. 1h, the lattice spacing of (100) plane was measured to be ~1.7 nm (Fig. 1i). Note that, the (100) lattice spacing refers to the intrinsic aperture size of TpBD-NH_2, which is reported to be around 1.6–2.3 nm [30].

Based on the above investigation, we understand that the synthesized TpBD-NH_2 nanosheets are ultrathin, crystalline, and carry abundant amino groups on their apertures. Amino groups render TpBD-NH_2 nanosheets excellent hydrophilicity and high chemical reactivity that not only can be fully dispersed in water (Fig. S4), but also provide an opportunity to be further chemically stitched.

3.2. Chemical stitch of TpBD-NH_2 nanosheets

TpBD-NH_2 nanosheets possessing abundant amino groups are expected to directly react with acyl chlorides of TMC. However, as the macrocyclic and conjugated structures of TpBD-NH_2 would lead to the steric hindrance effect, those amino groups are not able to straightforwardly react with acyl chlorides. We hereby introduced a highly efficient acylation catalyst, DMAP, to trigger the reaction, which is proven to be effective in forming highly cross-linked polymer networks when using low reactive monomers [32–35]. The TpBD-NH_2 nanosheets were activated by DMAP so that they could react with TMC at the immiscible oil-water interface. TMC with ultrahigh reactivity acted as a cross-linker to chemically stitch the amino nanosheets into a continuous and highly-aligned architecture of which the apertures are featuring the perpendicular orientation.

As shown in Fig. 2a and b, a very thin film was formed on an oil-water interface after a reaction duration of 30 s, which can be transferred, and then floated on water (Fig. 2c). The thin films were further deposited onto polyvinylidene fluoride macroporous substrates (PVDF, average pore size ~0.22 μm), and the underlying membrane macropores can be clearly seen, indicative of the ultrathin thicknesses (Fig. S5). The ultrathin nature of the thin film was further confirmed by the AFM, and its thickness was measured to be ~8.6 nm (Fig. 2d and e). The surface of such nanofilm was relatively hydrophobic as its WCA was determined to be ~77° (Fig. 2f). This result mainly originates from many hydrophobic aromatic rings in TMC introduced into the nanofilm backbone. The chemical compositions were verified by the FT-IR spectrum (Fig. 2g). Two characteristic stretching vibration peaks of C═C (1647 cm^{-1}) and C–N (1278 cm^{-1}) were detected, attributing to the TpBD-NH_2 backbone. A newly emerged stretching vibration peak of C═O (1609 cm^{-1}) was ascribed to the amide group after the reaction of TMC and TpBD-NH_2 nanosheets, evidencing the occurrence of the chemical stitching processes. It is notable that a very strong stretching vibration peak of C═O (1721 cm^{-1}) also emerged, suggesting the presence of a large number of acyl chlorides or even carboxyl groups (acyl chlorides after the hydrolysis) which originated from the unreacted TMC. These unreacted acyl chlorides anchored on the TpBD-NH_2 would reduce its original aperture size to some extent. Besides, the TpBD-NH_2 nanofilms may provide the active sites for further reaction with PIP to form PA matrices, which would be discussed later.

To further understand the chemical stitch process, we investigated the effect of the reaction time on the nanofilm thicknesses. As shown in Fig. 2h and S6, the thicknesses of nanofilms was increased with rising reaction time, and the nanofilm growth process can be divided into three stages. In the first stage, the thickness was increased sharply from 6.7 nm to 10 nm within 60 s, revealing a fast-reacting process that is similar to the conventional IP. In the second stage, the thickness was increased from 10 nm to 13.8 nm within 120 s, which is two times slower than that of the first stage. This is mainly because of the “self-limiting” effect, retarding the reaction. In the third stage, the thickness was increased from 13.8 nm to 17.8 nm within 420 s, which is 3.5 times slower than that of the second stage, demonstrating a much pronounced self-limiting effect.

In the light of above results, we understand the possible mechanism of the chemical stitch of TpBD-NH_2 nanosheets. The reaction of TpBD-NH_2 nanosheets and TMC was triggered by the DMAP, and thus the nanosheets can react with TMC at the interface instantly to form a primary nanofilm. Due to the large dimensions, planar structures, and irregular shapes of TpBD-NH_2 nanosheets, the promptly-formed primary nanofilm did not possess an integrated and continuous structure. The smaller sized TpBD-NH_2 nanosheets would thus continuously diffuse toward the interface for stitching the defects within the primary nanofilm. Ultimately, driven by such reaction-diffusion process, TpBD-NH_2 nanosheets were cross-linked by TMC to give an integrated and continuous film over the interface.

Owing to the high chemical reactivity of TMC, the TpBD-NH_2 nanosheets were rapidly stitched and the thickness of nanofilms was increased drastically at the early stage of the reaction (within 60 s). However, when the primary nanofilm became integrated and continuous, it would be very difficult for nanosheets to effectively contact and react with TMC as the reaction time exceeded 60s. That is, the reaction-diffusion process would be decelerated when the interface was wholly covered by the formed nanofilm, which is the self-limiting effect. This phenomenon is similar to the conventional IP, in which the reaction rate would be slowed down as the primary PA nanofilm became tight. At the last stage, the increase of the nanofilm thickness was significantly decelerated, because of the much pronounced self-limiting. Therefore, such distinctive self-limiting effect would endow TpBD-NH_2 nanofilm with ultrathin thicknesses, which is barely influenced by the prolonged reaction durations.

Besides, the TpBD-NH_2 nanofilm possesses a highly-aligned

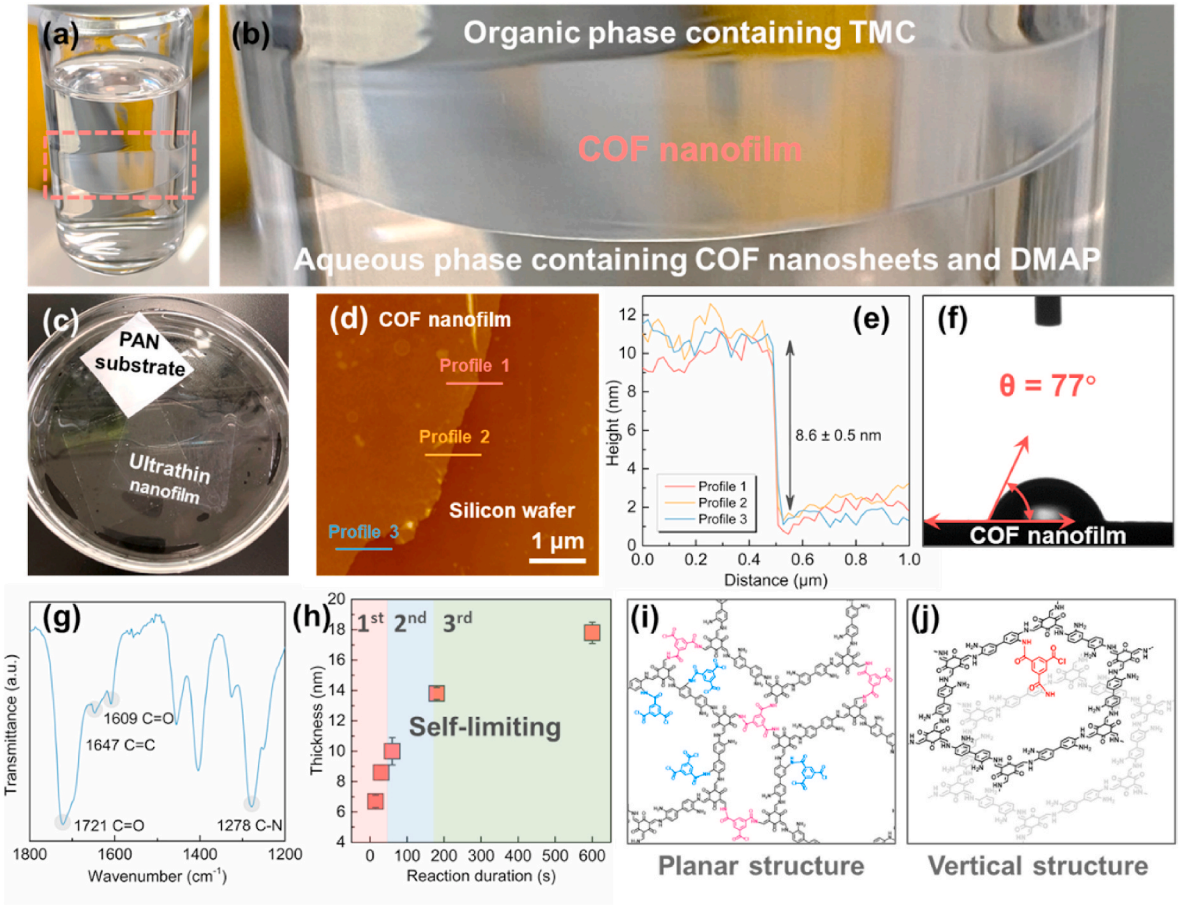

Fig. 2. Chemical stitch of TpBD-NH_2 nanosheets. (a) Digital image of a reaction-diffusion driven synthesis of TpBD-NH_2 nanofilms at an oil-water interface. (b) A magnified image from (a). (c) Digital image of a TpBD-NH_2 nanofilm floating on water. (d) AFM image of a TpBD-NH_2 nanofilm. (e) Height profiles of the TpBD-NH_2 nanofilm corresponding to the three lines marked in (d). (f) WCA of the TpBD-NH_2 nanofilm. (g) FT-IR spectrum of the TpBD-NH_2 nanofilm. (h) Variation of the thicknesses of TpBD-NH_2 nanofilms under different reaction durations. Schematic diagram of the TpBD-NH_2 nanofilm: (i) planar structure and (j) vertical structure.

microstructure (Scheme 1 and Fig. 2i and j). Considering that the thickness of TpBD-NH_2 nanosheets was measured to be ~4 nm, those nanofilms are merely composed of a few layers of nanosheets. For instance, a ~8.6 nm-thick TpBD-NH_2 nanofilm formed at 30 s is comprised of two layers of nanosheets. Therefore, we conclude that the TMC would regioselectively interlink the amino groups at both planar and vertical directions, allowing TpBD-NH_2 nanosheets to be directionally stitched at the confined interface with their intrinsic apertures face the organic solution (that is, the perpendicular direction). The nanofilm comprises two types of in-plane pores: the intrinsic apertures as well as newly formed pores, and the gaps among the edges of stitched adjacent nanosheets, which we term as "stitched gaps". The membranes possess these oriented pores are expected to offer the potential for achieving outstanding performance, and we thereby tried to directly use such nanofilms for separation. However, due to the large dimensions, planar structures, and irregular shapes of TpBD-NH_2 nanosheets, it is very difficult to form highly cross-linked nanofilms with sufficient mechanical strength. Therefore, the nanofilms obtained in current form would not be suitable to be directly used as separation membranes. Further works may focus on how to make the nanofilm robust enough to be capable of being applied for separation. Nonetheless, the chemical stitch is still expected as a simple and universal strategy for fabricating ultrathin and aligned COF membranes. We expect that other types of 2D COFs carrying sufficient reactive groups could also be suitable for our strategy, which would broaden the fabrication methodology for COF membranes.

3.3. Fabrication of TFN membranes

The highly-aligned TpBD-NH_2 nanofilms were in-situ embedded into PA matrices to give the TFN membranes. To make a comparison, two control membranes were also prepared. The PA membranes were fabricated from PIP and TMC to form pure PA matrices. The FreeCOF-PA membranes were fabricated by directly adding TpBD-NH_2 nanosheets into PIP solutions, in which the nanosheets were randomly embedded into PA matrices with an anisotropic alignment. All TFN membranes were composited onto PAN substrates (Fig. S7).

We used SEM to analyze the effects of TpBD-NH_2 on the morphologies of TFN membranes (Fig. 3a and b and S8). Interestingly, a patterned surface with a large number of crumples is clearly observed in COF-PA membrane (Fig. 3a). This unique morphology is quite similar to that of the "Turing structure", which is reported by Zhang and coworkers [36]. The intrinsic apertures and the stitched gaps of TpBD-NH_2 nanofilm would rectify the diffusion of PIP molecules toward the organic solutions, by which means the diffusion processes were significantly retarded, leading to the diffusion-difference-enabled crumpled patterns. By contrast, the surface of PA membrane exhibits a nodule-typed morphology which commonly exists in conventional PA-based NF membranes (Fig. 3b). This result supports that the highly-aligned TpBD-NH_2 functions as the rectifier and mediator in forming the PA matrices with the well-defined structures. Besides, the surface morphology of FreeCOF-PA membrane exhibits a leaf-like crumpled pattern, which is also created by the diffusion-difference effect (Fig. S8). In this case, however, the forming mechanism of the

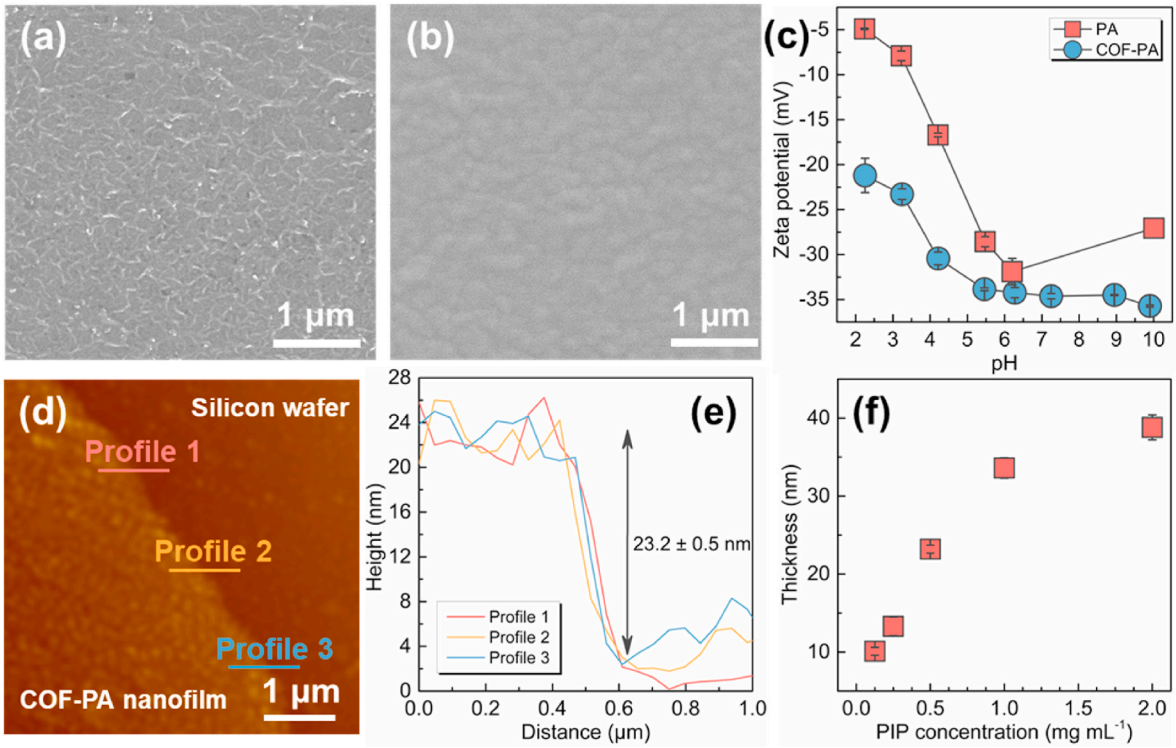

Fig. 3. Characterization of membranes. SEM images of the surface morphologies of (a) COF-PA and (b) PA membranes. (c) Zeta potentials of COF-PA and PA membranes. (d) AFM image of COF-PA membrane. (e) Height profiles of the COF-PA membrane corresponding to the three lines marked in (d). (f) Changes of the membrane thicknesses with PIP concentrations.

crumpled pattern is different from that of COF-PA membrane. The negatively charged TpBD-NH_2 can interact with the positively charged PIP, thus slowing down the diffusion of PIP [22,37]. Furthermore, the surface roughnesses of the COF-PA membrane (5.9 nm), the PA membrane (5.5 nm), and the FreeCOF-PA membrane (21.7 nm) are also supportive of above results (Fig. S9).

The membrane surface charging properties are shown in Fig. 3c. Both membranes demonstrated negatively charged surfaces in the neutral environment. This is because the high dosage of TMC used in this work would create residual acyl chlorides, which can be further converted into negatively charged carboxyl groups by the hydrolysis process when the freshly prepared membranes soaking/floating in water. Moreover, the COF-PA membrane bears more negative charges on the surface than the PA membrane. This is because the stitched TpBD-NH_2 nanosheets carry abundant acyl chlorides that may create a large number of carboxyl groups compared to those of PA membrane. Their chemical compositions are confirmed by the ATR-FTIR spectra (Fig. S10). WCAs of different membranes are shown in Fig. S11. The PA membrane was relatively hydrophobic, which is mainly due to the formation of a tight structure of PA matrix induced by the catalysis of DMAP. For the COF-PA membrane, the porous nature of TpBD-NH_2 would allow water droplet to easily penetrate and spread, thus rendering the TFN membrane reduced WCA and enhanced hydrophilicity compared to that of the PA membrane. However, such improvement was not significant, as the FreeCOF-PA membrane exhibited a higher hydrophilicity compared to that of COF-PA membrane. This is because the TpBD-NH_2 nanofilms is relatively hydrophobic as mentioned previously, and the high alignment would strengthen such property compared to that of randomly aligned TpBD-NH_2 in PA matrices. Besides, the WCAs of TFN membranes were slightly lower than that of the TpBD-NH_2 nanofilm. Because the TpBD-NH_2 nanofilms were fully encapsulated by the PA networks, the carboxyl groups derived from the hydrolysis of the acyl chlorides within the PA networks would slightly reduce the WCAs.

To illuminate the formation processes of the TFN membranes, we conducted the AFM analysis as shown in Fig. 3d, e and S12. The COF-PA membrane prepared at the PIP concentration of 0.5 mg mL^{-1} possessed a very thin thickness of ~23.2 nm, which is lower than that of the PA membrane (~27.8 nm) and the FreeCOF-PA membrane (~27.5 nm) (Fig. S12). This result suggests that the highly-aligned TpBD-NH_2 mediates the IP process by controlling the diffusion of PIP, resulting in reduced membrane thickness, which is consistent with the analysis discussed above.

We further investigated the effects of various PIP concentrations on the TFN membrane thicknesses and surface morphologies (Fig. 3f, S13, S14). With the PIP concentration raised from 0.125 to 1 mg mL^{-1}, the membrane thickness was increased from 10.1 nm to 33.6 nm. Such proportional increase indicates that the PIP molecules at low concentrations were easily penetrating through the intrinsic apertures and stitched gaps to react with TMC forming thin membranes. In comparison, the membrane formed at a high concentration of 2 mg mL^{-1} exhibited a similar thickness of 38.8 nm with the membrane formed at the concentration of 1 mg mL^{-1}. This phenomenon can be also ascribed to the rectification and mediation of the PIP diffusion. The oriented in-plane pores allowed the PIP molecules to penetrate through them in a homogeneous and controllable manner, leading to membranes with reduced thicknesses rather than the uncontrolled large thickness [38]. Moreover, all TFN membranes exhibited crumpled patterns (Fig. S14). As the concentrations increased, the feature size of those crumpled patterns was becoming much larger, indicative of the gradually strengthened diffusion-difference-enabled properties. It is notable that the TpBD-NH_2 inside PA matrices also possess highly-aligned structures, because they were in-situ encapsulated during the formation of PA matrices. Besides, the thicknesses of TpBD-NH_2 nanofilms would maintain unchanged during the formation of PA matrices. This is because the increase of the nanofilm thicknesses is contained by the much pronounced self-limiting effect, and the PIP molecules have much higher chemical reactivity compared to that of the TpBD-NH_2. Although the TFN membranes originated from different PIP concentrations have

various crumpled morphologies, each of them substantially possessing homogeneous intrinsic thicknesses [36]. Therefore, since it is difficult to directly obtain the exact masses of stitched TpBD-NH_2 and PA matrices, based on above reasons, we used the ratios of thicknesses between the TpBD-NH_2 nanofilms and COF-PA membranes to estimate the proportions of the nanofillers inside matrices. The proportions can be approximately calculated as ~85%, 65%, 37%, 26% and 22% for PIP concentrations of 0.125, 0.25, 0.5, 1 and 2 mg mL^{-1}, respectively, demonstrating very high loading densities.

On the basis of the analyses above, we can conclude that the highly-aligned TpBD-NH_2 is capable of acting a mediator during the formation of PA matrices. The oriented in-plane pores could promote the PIP molecules diffuse them in a controlled fashion, thus not only leading to the ultrathin membrane thicknesses, but also creating patterned surfaces. This distinctive feature makes our TFN membranes quite different from other mixed matrix membranes, of which the nanofillers are merely used as the performance enabler for the improvement of the separation performances.

3.4. Desalination performance

To illustrate the structure-performance relationship, we investigated the effects of various PIP concentrations on the water permeance and Na_2SO_4 rejection of the TFN membranes. As shown in Fig. 4a, as the PIP concentration was raised from 0.125 to 0.5 mg mL^{-1}, the water permeances were decreased from 34.4 to 6.0 L m^{-2} h^{-1} bar^{-1}, whilst the Na_2SO_4 rejections were increased from 52.6% to 98.1%. At the PIP concentrations of 0.125 mg mL^{-1}, as referred above, the proportion of TpBD-NH_2 is ~85%. The insufficient PIP concentration could not be able to form an integrated PA matrix, leading to deficient Na_2SO_4 rejection. Thereby, the separation process was considered to be dominated by the intrinsic apertures and stitched gaps of TpBD-NH_2 nanofilms which are considered slightly larger than that of PA matrices. With the PIP concentration further raised to 1 and 2 mg mL^{-1}, the Na_2SO_4 rejections were almost maintained at a stable level higher than 98%, while the water permeances were decreased to 2.8 L m^{-2} h^{-1} bar^{-1}. The low permeances and high rejections resulted from the increased thicknesses and much tighter membrane structures. Although our TFN membranes have very high nanofiller loading densities, high Na_2SO_4 rejections (exceeded 98%) were realized. This is quite different to that of other TFN membranes, which would attribute to the excellent compatibility between TpBD-NH_2 and PA matrices. A large amount of unreacted acyl chlorides were decorated on the TpBD-NH_2 nanofilms as confirmed by the FT-IR spectra. Such reactive groups functioned as the anchoring sites for further reacting with introduced PIP molecules. Therefore, the PA networks are chemically bonded with the TpBD-NH_2 nanofilms that provide the strong compatibility, for which reason the TFN membranes are featured with much tighter structures and thus expected to give better desalination performances.

We then studied the desalination performances of different membranes on various salts. As shown in Fig. 4b, four inorganic salts of Na_2SO_4, $MgSO_4$, NaCl and $MgCl_2$ were selected as model solutes for evaluating the desalination performances of various TFN membranes. The rejection characteristics of membranes all followed the order: Na_2SO_4 > $MgSO_4$ > NaCl > $MgCl_2$ (Figure 4b and S15). The size exclusion and the Donnan effect are widely accepted as the two main separation mechanism for the NF processes [39]. In this case, alongside the size exclusion, the Donnan effect plays an important role in sieving different salts because of the strong negatively charged membranes surfaces as demonstrated before. Due to the strong electrostatic repulsion, the divalent anions underwent higher rejections than monovalent anions. Meanwhile, because of the strong electrostatic attraction, the divalent cations possessed higher affinity to the charged membranes than that of monovalent cations. In addition, the divalent ions possess much larger hydrated radiuses than those of monovalent ions, thus resulting in higher rejections of divalent ions. Note that, for the FreeCOF-PA membrane, the rejection of $MgCl_2$ was slightly higher than that of NaCl, which is probably due to the perturbation originating from reduced desalination performance compared to those of COF-PA and PA membranes. Based on the results above, we understand the pore structures inside the TFN membranes. After the formation of PA matrices, there are two types of pores in the TFN membranes. The first one is the micropores of PA networks, of which the pore sizes are typically smaller than 1 nm. The second one is the intrinsic pores of TpBD-NH_2 (slightly reduced by the grafted acyl chlorides), of which the pore sizes are less than 1.7 nm.

Considering that the rejection difference between Na_2SO_4 and NaCl is quite obvious, we thereby further investigated the relationship

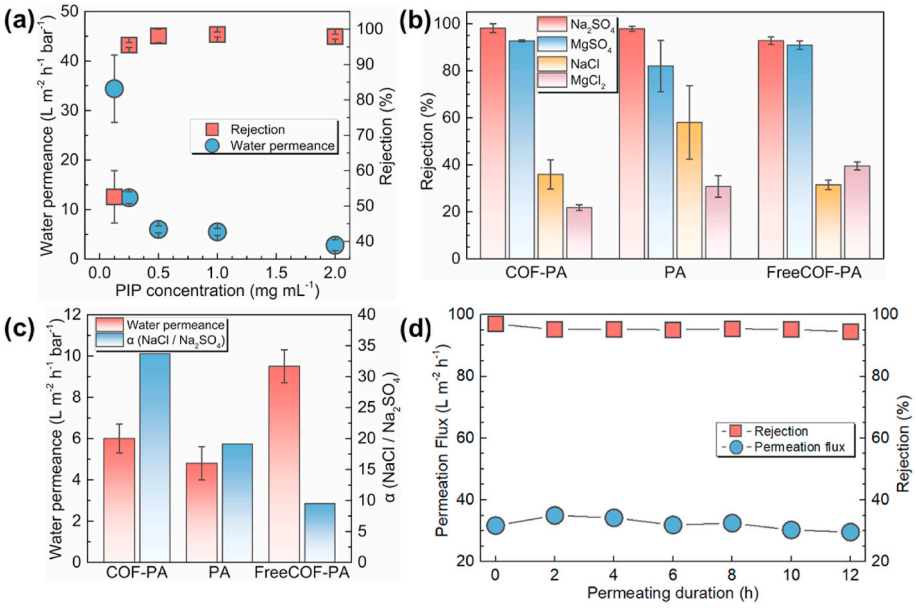

Fig. 4. Desalination performances. (a) Variation of water permeance and Na_2SO_4 rejection under different PIP concentrations. (b) Inorganic salts rejection of different membranes. (c) Water permeance and separation factor of different membranes. (d) Variation of permeation flux and Na_2SO_4 rejection under a permeating period of 12 h.

between water permeance and the separation factor to NaCl and Na_2SO_4 (Fig. 4c). The sieving characteristics between divalent ions and monovalent ions are of great significance to the NF processes, and such feature would have potential impacts over various real-world applications including hard water softening and the extraction of lithium from brines. The separation factor of COF-PA membrane tops a high value of 33.7, much higher than those of the PA membrane (19.1) and the FreeCOF-PA membrane (9.5). The stitched TpBD-NH_2 possesses slightly larger pore sizes than those of PA matrices that allow NaCl to easily pass through while Na_2SO_4 to be blocked. Moreover, the stitched TpBD-NH_2 renders membrane surface strong negative charges, enhancing the repulsion of Na_2SO_4. Once again, this result is supportive of the important role of highly-aligned TpBD-NH_2 in the separation process. For the water permeance, the COF-PA membrane (6.0 L m^{-2} h^{-1} bar^{-1}) and the FreeCOF-PA membrane (9.5 L m^{-2} h^{-1} bar^{-1}) exhibited larger water permeances than the PA membrane (4.8 L m^{-2} h^{-1} bar^{-1}), as a result of the additional water channels created by the TpBD-NH_2. However, the water permeance of FreeCOF-PA membrane is higher than that of the COF-PA membrane. This is mainly because the relative hydrophobicity of highly-aligned TpBD-NH_2 did not have a high affinity toward water molecules, leading to a relatively reduced water permeance. Although, the higher water permeance is realized in the FreeCOF-PA membrane, its separation factor is deeply compromised compared to that of the COF-PA membrane. Such performance tendency is consistent with those of many other TFN membranes reported elsewhere, by which means the improvement of water permeance may probably derive from the undermining of the solute selectivity to some extent. In this work, owing to the excellent compatibility and the preferential orientation of embedded TpBD-NH_2, the water permeance as well as the selectivity were simultaneously boosted, which is distinctive to many other similar works [21,22]. We also investigated the desalination stability of our membrane. As shown in Fig. 4d, the permeation flux and the rejection were stable during a cross-flow filtration period of 12 h, demonstrating its outstanding desalination performance.

4. Conclusions

In summary, we reported an unusual TFN membrane fabrication strategy that embeds highly-aligned TpBD-NH_2 nanosheets into the PA matrices, enabling highly-efficient desalination. Nanofilms were formed by a reaction-diffusion driven synthesis (RDDS) in which the reactive TpBD-NH_2 nanosheets were chemically stitched into a preferentially oriented nanofilm. The PA matrices were directly grown on the preformed TpBD-NH_2 nanofilm so that they were covalently linked and thus entirely fused. The highly-aligned TpBD-NH_2 not only functioned as a mediator for controllable synthesis of the ultrathin and patterned PA matrices, but also worked as an enabler for effectively sieving of Na_2SO_4 and NaCl. Benefiting from the excellent compatibility as well as the perpendicular alignment of in-plane pores in COFs, the boosted water permeance and enhanced selectivity could be simultaneously realized. This work not only provides a unique strategy for fabricating high-performance TFN membranes, but also demonstrates an efficient method to perpendicularly align COF nanosheets, which is very important for the usages of COFs in many different fields.

Author statement

Zhe Zhang: Investigation, Methodology, Data curation, Writing-Original Draft. Congcong Yin: Investigation, Data curation. Guanghui Yang: Investigation, Data curation. Ankang Xiao: Investigation, Data curation. Xiansong Shi: Investigation, Data curation. Weihong Xing: Supervision, Funding acquisition. Yong Wang: Supervision, Conceptualization, Writing-Review & Editing, Funding acquisition. All authors have approved to the final version of the manuscript.

Declaration of competing interest

The authors declare that they have no known competing financial interests or personal relationships that could have appeared to influence the work reported in this paper.

Acknowledgements

This work was financially supported by the National Science Foundation of China (21825803, 21921006). We also thank the Program of Excellent Innovation Teams of Jiangsu Higher Education Institutions and the Project of Priority Academic Program Development of Jiangsu Higher Education Institutions (PAPD).

Appendix A. Supplementary data

Supplementary data to this article can be found online at https://doi.org/10.1016/j.memsci.2020.118754.

References

[1] M.A. Shannon, P.W. Bohn, M. Elimelech, J.G. Georgiadis, B.J. Marinas, A. M. Mayes, Science and technology for water purification in the coming decades, Nature 452 (2008) 301–310.
[2] J.R. Werber, C.O. Osuji, M. Elimelech, Materials for next-generation desalination and water purification membranes, Nat. Rev. Mater. 1 (2016) 1–15.
[3] S.P. Nunes, P.Z. Culfaz-Emecen, G.Z. Ramon, T. Visser, G.H. Koops, W. Jin, M. Ulbricht, Thinking the future of membranes: perspectives for advanced and new membrane materials and manufacturing processes, J. Membr. Sci. 598 (2020) 117761.
[4] A. Lee, J.W. Elam, S.B. Darling, Membrane materials for water purification: design, development, and application, Environ. Sci. J. Integr. Environ. Res.: Water Res. Technol. 2 (2016) 17–42.
[5] N. García Doménech, F. Purcell-Milton, Y.K. Gun'ko, Recent progress and future prospects in development of advanced materials for nanofiltration, Mater. Today Commun. 23 (2020) 100888.
[6] Y. Ji, W. Qian, Y. Yu, Q. An, L. Liu, Y. Zhou, C. Gao, Recent developments in nanofiltration membranes based on nanomaterials, Chin. J. Chem. Eng. 25 (2017) 1639–1652.
[7] M.J.T. Raaijmakers, N.E. Benes, Current trends in interfacial polymerization chemistry, Prog. Polym. Sci. 63 (2016) 86–142.
[8] S. Wang, F. Zhang, J.B. Fan, Interfacial polymerization: from chemistry to functional materials, Angew. Chem. Int. Ed. (2020), https://doi.org/10.1002/anie.201916473.
[9] E.L. Wittbecker, P.W. Morgan, Interfacial polycondensation. I, J. Polym. Sci. 40 (1959) 289–297.
[10] P.W. Morgan, S.L. Kwolek, Interfacial polycondensation. II. Fundamentals of polymer formation at liquid interfaces, J. Polym. Sci. 40 (1959) 299–327.
[11] H.B. Park, J. Kamcev, L.M. Robeson, M. Elimelech, B.D. Freeman, Maximizing the right stuff: the trade-off between membrane permeability and selectivity, Science 356 (2017) eaab0530.
[12] Z. Yang, H. Guo, C.Y. Tang, The upper bound of thin-film composite (TFC) polyamide membranes for desalination, J. Membr. Sci. 590 (2019) 117297.
[13] W.J. Lau, S. Gray, T. Matsuura, D. Emadzadeh, J. Paul Chen, A.F. Ismail, A review on polyamide thin film nanocomposite (TFN) membranes: history, applications, challenges and approaches, Water Res. 80 (2015) 306–324.
[14] B.-H. Jeong, E.M.V. Hoek, Y. Yan, A. Subramani, X. Huang, G. Hurwitz, A. K. Ghosh, A. Jawor, Interfacial polymerization of thin film nanocomposites: a new concept for reverse osmosis membranes, J. Membr. Sci. 294 (2007) 1–7.
[15] H. Wu, B. Tang, P. Wu, Optimizing polyamide thin film composite membrane covalently bonded with modified mesoporous silica nanoparticles, J. Membr. Sci. 428 (2013) 341–348.
[16] H. Sun, P. Wu, Tuning the functional groups of carbon quantum dots in thin film nanocomposite membranes for nanofiltration, J. Membr. Sci. 564 (2018) 394–403.
[17] R. Hu, R. Zhang, Y. He, G. Zhao, H. Zhu, Graphene oxide-in-polymer nanofiltration membranes with enhanced permeability by interfacial polymerization, J. Membr. Sci. 564 (2018) 813–819.
[18] M. Wu, T. Ma, Y. Su, H. Wu, X. You, Z. Jiang, R. Kasher, Fabrication of composite nanofiltration membrane by incorporating attapulgite nanorods during interfacial polymerization for high water flux and antifouling property, J. Membr. Sci. 544 (2017) 79–87.
[19] M.-Q. Ma, C. Zhang, C.-Y. Zhu, S. Huang, J. Yang, Z.-K. Xu, Nanocomposite membranes embedded with functionalized MoS_2 nanosheets for enhanced interfacial compatibility and nanofiltration performance, J. Membr. Sci. 591 (2019) 117316.
[20] Y. Gong, S. Gao, Y. Tian, Y. Zhu, W. Fang, Z. Wang, J. Jin, Thin-film nanocomposite nanofiltration membrane with an ultrathin polyamide/UIO-66-NH_2 active layer for high-performance desalination, J. Membr. Sci. 600 (2020) 117874.

[21] C. Wang, Z. Li, J. Chen, Z. Li, Y. Yin, L. Cao, Y. Zhong, H. Wu, Covalent organic framework modified polyamide nanofiltration membrane with enhanced performance for desalination, J. Membr. Sci. 523 (2017) 273–281.
[22] N.A. Khan, J. Yuan, H. Wu, T. Huang, X. You, A.U. Rahman, C.S. Azad, M.A. Olson, Z. Jiang, Covalent organic framework nanosheets as reactive fillers to fabricate free-standing polyamide membranes for efficient desalination, ACS Appl. Mater. Interfaces 12 (2020) 27777–27785.
[23] L. Zhang, M. Zhang, J. Lu, A. Tang, L. Zhu, Highly permeable thin-film nanocomposite membranes embedded with PDA/PEG nanocapsules as water transport channels, J. Membr. Sci. 586 (2019) 115–121.
[24] Z. Sun, Q. Wu, C. Ye, W. Wang, L. Zheng, F. Dong, Z. Yi, L. Xue, C. Gao, Nanovoid membranes embedded with hollow zwitterionic nanocapsules for a superior desalination performance, Nano Lett. 19 (2019) 2953–2959.
[25] Y. Qin, H. Liu, Y. Liu, M. Chen, K. Chen, Y. Huang, C. Xiao, Design of a novel interfacial enhanced GO-PA/APVC nanofiltration membrane with stripe-like structure, J. Membr. Sci. 604 (2020) 118064.
[26] X. You, T. Ma, Y. Su, H. Wu, M. Wu, H. Cai, G. Sun, Z. Jiang, Enhancing the permeation flux and antifouling performance of polyamide nanofiltration membrane by incorporation of PEG-POSS nanoparticles, J. Membr. Sci. 540 (2017) 454–463.
[27] C.S. Diercks, O.M. Yaghi, The atom, the molecule, and the covalent organic framework, Science 355 (2017), eaal1585.
[28] K. Geng, T. He, R. Liu, S. Dalapati, K.T. Tan, Z. Li, S. Tao, Y. Gong, Q. Jiang, D. Jiang, Covalent organic frameworks: design, synthesis, and functions, Chem. Rev. (2020), https://doi.org/10.1021/acs.chemrev.9b00550.
[29] S. Chandra, S. Kandambeth, B.P. Biswal, B. Lukose, S.M. Kunjir, M. Chaudhary, R. Babarao, T. Heine, R. Banerjee, Chemically stable multilayered covalent organic nanosheets from covalent organic frameworks via mechanical delamination, J. Am. Chem. Soc. 135 (2013) 17853–17861.
[30] M.S. Lohse, T. Stassin, G. Naudin, S. Wuttke, R. Ameloot, D. De Vos, D.D. Medina, T. Bein, Sequential pore wall modification in a covalent organic framework for application in lactic acid adsorption, Chem. Mater. 28 (2016) 626–631.
[31] S. Kandambeth, A. Mallick, B. Lukose, M.V. Mane, T. Heine, R. Banerjee, Construction of crystalline 2D covalent organic frameworks with remarkable chemical (acid/base) stability via a combined reversible and irreversible route, J. Am. Chem. Soc. 134 (2012) 19524–19527.
[32] J. Cheng, Z. Zhang, W. Shi, R. Zhang, B. Zhang, X. Bao, Y. Guo, F. Cui, A novel polyester composite nanofiltration membrane prepared by interfacial polymerization catalysed by 4-dimethylaminopyridine: enhanced the water permeability and anti-fouling ability, Polymer 153 (2018) 24–32.
[33] J. Qin, S. Lin, S. Song, L. Zhang, H. Chen, 4-Dimethylaminopyridine promoted interfacial polymerization between hyperbranched polyesteramide and trimesoyl chloride for preparing ultralow-pressure reverse osmosis composite membrane, ACS Appl. Mater. Interfaces 5 (2013) 6649–6656.
[34] R. Zhang, S. Yu, W. Shi, w. Wang, X. Wang, Z. Zhang, L. Li, B. Zhang, X. Bao, A novel polyesteramide thin film composite nanofiltration membrane prepared by interfacial polymerization of serinol and trimesoyl chloride (TMC) catalyzed by 4-dimethylaminopyridine (DMAP), J. Membr. Sci. 542 (2017) 68–80.
[35] H. Peng, W.H. Zhang, W.S. Hung, N. Wang, J. Sun, K.R. Lee, Q.F. An, C.M. Liu, Q. Zhao, Phosphonium modification leads to ultrapermeable antibacterial polyamide composite membranes with unreduced thickness, Adv. Mater. 32 (2020) 2001383.
[36] Z. Tan, S. Chen, X. Peng, L. Zhang, C. Gao, Polyamide membranes with nanoscale Turing structures for water purification, Science 360 (2018) 518–521.
[37] Z. Zhang, X. Shi, R. Wang, A. Xiao, Y. Wang, Ultra-permeable polyamide membranes harvested by covalent organic framework nanofiber scaffolds: a two-in-one strategy, Chem. Sci. 10 (2019) 9077–9083.
[38] J. Yuan, M. Wu, H. Wu, Y. Liu, X. You, R. Zhang, Y. Su, H. Yang, J. Shen, Z. Jiang, Covalent organic framework-modulated interfacial polymerization for ultrathin desalination membranes, J. Mater. Chem. 7 (2019) 25641–25649.
[39] W.J. Lau, A.F. Ismail, N. Misdan, M.A. Kassim, A recent progress in thin film composite membrane: a review, Desalination 287 (2012) 190–199.